Catalysis Today xxx (xxxx) xxx

Contents lists available at ScienceDirect

Catalysis Today

journal homepage: www.elsevier.com/locate/cattod

The direct synthesis of hydrogen peroxide over Au and Pd nanoparticles: A DFT study

Nishtha Agarwal [a], Liam Thomas [a], Ali Nasrallah [a], Mala A. Sainna [a], Simon J. Freakley [b], Jennifer K. Edwards [a], C. Richard A. Catlow [a], Graham J. Hutchings [a], Stuart H. Taylor [a], David J. Willock [a,*]

[a] Cardiff Catalysis Institute, School of Chemistry, Cardiff University, Cardiff, CF10 3AT, UK
[b] Department of Chemistry, University of Bath, Claverton Down, Bath, BA2 7AY, UK

ARTICLE INFO

Keywords:
DFT calculations
Nanoparticles
Oxidation
Catalysis
Hydrogenperoxide
Reaction scheme

ABSTRACT

Catalysts consisting of Au, Pd and their alloys have been shown to be active oxidation catalysts. These materials can use dioxygen or hydrogen peroxide as the oxidant with CO and activated organic molecules using O_2(g) while more challenging cases, such as methane to partial oxygenates, relying on H_2O_2. Although H_2O_2 is a green oxidant, the incorporation of dioxygen greatly reduces overall cost and so there is an incentive to find new ways to reduce the reliance on H_2O_2. In this study we use DFT calculations to discuss the direct synthesis of H_2O_2 from H_2(g) and O_2(g) and use this understanding to identify the important surface species derived from dioxygen. We cover the adsorption of oxygen, hydrogen and water to model Au and Pd nanoclusters and the oxidation of the metals, since reduction of any oxides formed will consume H_2. We then turn to the production of a surface hydroperoxy species; the first step in the synthesis of H_2O_2. This can occur *via* hydrogenation of O_2(ads) with H_2(ads) or *via* protonation of O_2(ads) by solvent water. Both routes are found to be energetically reasonable, but the latter is likely to be favoured under experimental conditions.

1. Introduction

Gold and Palladium nanoparticles and their alloys have shown remarkable selectivity in a series of oxidation reactions over the last few decades [1,2]. The range of oxidation processes is very broad, from the removal of CO from waste gas streams to selective oxidations in organic chemistry and a similar range of proposed oxidation mechanisms have been put forward. Two main oxygen sources have been used depending on the specific chemistry required these are dioxygen and hydrogen peroxide. Clearly, processes that can employ dioxygen have an economic benefit over H_2O_2 as a stoichiomentric oxidant. Accordingly, there is interest in identifying how dioxygen can be employed more broadly. A promising link is to study the direct synthesis of H_2O_2 from H_2(g) and O_2(g), for which AuPd alloy catalyst/support combinations have been optimised [3,4]. In this contribution we begin with a brief survey of oxidation chemistry using gold and palladium nanoparticles and then present new results detailing DFT calculations on the reaction of H_2(g) and O_2(g) over Au and Pd using clusters of 38 atoms to represent metal particles at the nanometre scale.

For the case of Au, low temperature CO oxidation is the most widely studied reaction [5,6] with important applications in pollution control and the removal of unwanted CO from hydrogen feed streams *via* the preferential oxidation of CO with O_2 (PROX) for ammonia synthesis and fuel cell applications [7]. It was quickly realised that the size of the Au catalyst particles was critical for CO oxidation activity, with particles below 5 nm being required. Fundamental DFT calculations contributed to our understanding of the oxidation mechanisms showing that even isolated Au_{10} clusters are capable of activating O_2 by transfer of electron density to the molecule [8]. Cluster size effects were also investigated using model experimental systems under ultra-high vacuum. Goodman and co-workers, using a combination of STM and elevated pressure kinetics for Au supported on single crystal surfaces of TiO_2, suggested that particles containing only two atomic layers were important in CO oxidation [9]. Landman and co-workers used a soft landing approach to deposit Au clusters with controlled size on well-defined MgO surfaces, concluding that significant CO oxidation activity could be seen for clusters as small as Au_8 [10]. In parallel DFT calculations they found that while CO adsorbs on metallic facets of the nanoparticles, O_2 is activated

* Corresponding author.
E-mail address: willockdj@cardiff.ac.uk (D.J. Willock).

https://doi.org/10.1016/j.cattod.2020.09.001
Received 16 April 2020; Received in revised form 16 July 2020; Accepted 1 September 2020
Available online 10 September 2020
0920-5861/

at the edge sites of the clusters in contact with the oxide support [11]. AuPd alloy catalysts supported on silica have also shown low temperature (300 K) CO oxidation activity [12]. However, for the most active Au catalysts, the oxidation of CO is thought to involve the activation of oxygen at the interface of the nanoparticles and reducible supports [13] (TiO_2 [14], FeO_x [15,16], CeO_2 [17]) with models showing that oxygen can be delivered in a Mars-van Krevelen (MvK) process [18,19]. There is a barrier to removal of lattice oxygen in this MvK pathway, so that at very low temperatures (around 130 K) CO oxidation using Au/TiO_2 will revert to the Au only mechanism seen on non-reducible supports [20]. The important influence of supports on the reactivity of Au nanoparticles has recently been reviewed [21].

Both Au and Pd nanoparticles and their alloys have been shown to catalyse aldehyde and alcohol oxidations. Au/C catalysts have been shown to be superior to Pt/C for the oxidation of aldehydes to carboxylic acids in water [22]. Tsukuda and co-workers also showed that activated alcohols with a phenyl functional group substituent at the carbon atom of the alcohol can be converted to aldehydes with dioxygen as the oxidising agent using colloidal Au nanoparticle catalysts stabilised by poly (*N*-vinyl-2-pyrrolidone) (PVP), provided that a base is included in the aqueous reaction mixture [23]. In this work colloidal Au-PVP catalysts with a 1.3 nm diameter showed a 10^3 fold higher rate than that of larger particles (9.5 nm) whereas Pd-PVP nanoparticles showed little difference in rate as a function of size. The Au-PVP catalysed reactions also showed an isotopic effect that suggested the rate limiting step is the cleavage of the C—H bond at the alcohol carbon atom. These observations led to the proposal that the Au-PVP catalysts operate in a different way to the Pd-PVP nanoparticles. For the case of Pd supported on hydroxyapatite, it has been proposed that the conversion of the alcohol takes place on Pd° nanoparticles with the H atoms abstracted from the alcohol as surface hydride species, these are then removed by oxygen in the form of hydrogen peroxide [24]. The Pd-PVP data seems to follow the same mechanism. On the other hand, Tsukuda proposed that the strong size dependence of activity with Au-PVP colloidal catalysts stems from the ability of small Au particles to activate dioxygen to form surface superoxo (O_2^-) species, which have the ability to abstract H atoms from the co-adsorbed alcohol to achieve the oxidation. As the generation of the superoxo species is dependent on the Au nanoparticle size this route allows the observed rate enhancement to be understood. The gas phase oxidation of alcohols such as propanol, butanol, pentanol to aldehydes using Au supported on silica [25] may also follow a similar mechanism. For solution phase oxidation of glycerol Neurock, Davis and co-workers have also used labelling experiments combined with DFT calculations, to suggest that the oxidation of alcohols to acids at high pH actually involves hydroxide ions in the oxidation step, and that the role of dioxygen is to replenish these hydroxide ions on the catalyst surface [26]. Au-Pd alloyed nanoparticles have also shown high activities in the solvent free oxidation of primary alcohols with O_2 as the stoichiometric oxidant, with turn-over frequencies around 25 times greater than similar catalysts using either of the pure metals [27]. In this work particles with Au core and Pd shell structures were identified by STEM-XEDS mapping of the active nanoparticles.

Alkene oxidation of cycloalkenes can also be catalysed by Au/C with dioxygen as the oxygen donor using polar solvents or in solvent free conditions [28,29]. In this case dioxygen is brought into a radical reaction scheme, following an initial C—H homolytic bond cleavage in the position β to the double bond to produce an allylic radical [30]. More challenging alkene substrates, such as propene, require the co-feeding hydrogen [31]. The suggested mechanisms for epoxidation here involve hydrogen peroxide or hydroperoxyl species that are generated and used *in situ*, with the nanoparticles supported on a material with epoxidation catalysing sites such as anatase TiO_2, or porous titania containing materials like TS-1 [32,33].

We have also shown that nanoparticles of AuPd alloys are active catalysts for the oxidation of methane to partial oxidation products, particularly methanol. Initially, using nanoparticles supported on titania [34,35], it appeared that this reaction required the use of hydrogen peroxide as oxidant, and since the current market price of hydrogen peroxide is greater than methanol this imposes unacceptable costs on the process. However, recently we have demonstrated that, by using a combination of dioxygen and small amounts of hydrogen peroxide as a radical initiator, around 70 % of the partial oxidation products generated when methane is reacted over AuPd colloidal catalysts contain oxygen atoms derived from the dissolved O_2 [36]. This implies that, once the radical oxidation process is set in train, dioxygen can be incorporated into the product, making the process more efficient and cost effective.

It is interesting to reflect that each of these catalytic reactions make use of similar metal nanoparticles but there is a range of different ways that the oxidising species is derived. In both the alkene oxidation and methane partial oxidation examples, AuPd catalysts allow for the transformation of oxygen into an oxidising species with the electrophilic oxidation and radical chemistry characteristics of hydrogen peroxide. Indeed, one of the most important reactions that has been demonstrated with AuPd nanoparticles is their use to generate hydrogen peroxide directly from hydrogen and oxygen [37–39]. Hydrogen peroxide is an attractive chemical oxidant as the side product from the breakdown of H_2O_2 during oxidation reactions is simply water, making it a green alternative to other oxidants such as iodates, chromate or permanganate. The current industrial method for H_2O_2 synthesis relies on the sequential hydrogenation and oxidation of an alkyl anthraquinone, which has the advantage of avoiding the potential for explosive contact between hydrogen and oxygen [40]. This produces large quantities of highly concentrated hydrogen peroxide (up to 70 %), that has to be transported and then diluted locally to usable levels. The requirements for direct production of hydrogen peroxide to become economically viable in competition with the existing process have been discussed with the conclusion that small scale (10 kt per year) for on-site usage would be key [41]. Local direct production that respects the flammability compositions of the reagents would have a number of benefits, but the catalytic efficiency is hampered by side reactions between hydrogen and oxygen to produce water directly and the decomposition of H_2O_2 to water [42]. One of the important discoveries for the development of supported AuPd alloy catalysts is that acid pre-treatment of carbon supports can virtually switch off the hydrogenation of H_2O_2 to water, and so greatly improve the reaction selectivity with respect to H_2 utilisation [43].

Lunsford and co-workers have carried out mechanistic investigation into direct synthesis of H_2O_2 using Pd notionally supported on silica. However, their conclusions were that the active catalytic species is colloidal Pd [44] or $PdCl_2(aq)$ [45] formed in the aqueous reaction mixture. They note that isotopic labelling experiments demonstrate that there is no scrabbling of an $^{18}O_2$, $^{16}O_2$ mixture in the H_2O_2 produced, indicating that oxygen dissociation occurs irreversibly and will only lead to the production of water. In later work using ethanol as solvent they found that supported metallic Pd^0 was the active state of the metal and that oxidised Pd nanoclusters, PdO produce only water [46]. The stability of hydrogen peroxide in the reaction using supported AuPd alloy nanoparticles has been linked to the isoelectric point of the support [47]. The AuPd/C catalysts do not generate solution phase colloidal particles and operate as reusable heterogeneous catalysts in aqueous solution without the need for additional halide or acid [48]. Mechanistically, the production of hydrogen peroxide from O_2 and H_2 can be viewed as the hydrogenation of oxygen over the metal catalysts: [49,47]

$$M + O_2(sol) = M\text{-}O_2(ads) \quad (1)$$

$$M + H_2(sol) = M\text{-}H_2(ads) \quad (2)$$

$$M\text{-}O_2(ads) + M\text{-}H_2(ads) = M\text{-}O_2H(ads) + M\text{-}H\ (ads) \quad (3)$$

$$M\text{-}O_2H(ads) + M\text{-}H\ (ads) = 2\ M + H_2O_2(sol) \quad (4)$$

Here oxygen and hydrogen gases dissolved in the solvent are adsorbed to the surface metal sites (M) in steps 1 and 2. Hydrogen is then dissociated and added directly to the adsorbed oxygen molecule (steps 3 and 4). Experimentally a roughly 1:1 M ratio of O_2(g) and H_2(g) is used, with the partial pressures held outside of the lower bound of the explosive limit for this gas mixed with CO_2(g) as the gas phase diluent [3]. The use of CO_2 as a diluent has the added advantage that it partially dissolves in the reaction mixture forming carbonic acid which stabilises the H_2O_2 produced in the reaction against further reaction to H_2O. We note that the Henry constants for O_2 and H_2 in water under standard conditions are of similar magnitude [50] (O_2: 1.3×10^{-5} mol m^{-3} Pa^{-1}, H_2: 7.7×10^{-6} mol m^{-3} Pa^{-1}) and so dissolved gases in solution in the correct stoichiometry should be present.

An alternative view has also been put forward based on a redox mechanism reminiscent of the electrochemical production of hydrogen peroxide, [51,52] following:

$$M + O_2(sol) = M^+\text{-}O_2^-(ads) \quad (5)$$

$$M + M^+\text{-}O_2^-(ads) + H_2O(sol) = M^+\text{-}OOH^-(ads) + M^+\text{-}OH^-(ads) \quad (6)$$

$$M^+\text{-}OOH^{--}(ads) + H_2O(sol) = M^+\text{-}OH^-(ads) + H_2O_2(sol) \quad (7)$$

$$2\ M^+\text{-}OH^-(ads) + H_2(sol) = 2\ M + H_2O(sol) \quad (8)$$

Here the surface is partially oxidised by the adsorbed molecular oxygen to produce a surface superoxide species (step 5). This is then protonated by solvent water or acid to form a surface hydroperoxide anion (step 6), which is itself protonated to form hydrogen peroxide (step 7). The role of the hydrogen reagent is now to reduce the two metal sites that have been oxidised in the preceding steps and restore the metal and solvent to complete the catalytic cycle (step 8).

This reaction scheme also points toward the possibility that the metal particle could be oxidised by the oxygen dissolved in the reaction mixture and then hydrogen is consumed to reduce the particle back to the metallic state producing water. This is a side reaction that will also decrease the efficiency of hydrogen peroxide production with respect to the hydrogen reagent.

In this contribution we use a DFT modelling approach to consider the adsorption of oxygen to model nanoparticles of Au and Pd and then compare the energetic profiles for particle oxidation and for the first step in the two proposed routes to hydrogen peroxide.

2. Methodology

All calculations were performed using the Vienna Ab initio Simulation Package (VASP) [53–56]. Metal particles containing 38 atoms (generically M_{38}, with M = Au, Pd or a specified stoichiometry in a core-shell structure) in a truncated octahedral geometry (Fig. 1) were placed within a cubic periodic box of 25 Å on a side. A plane wave cut-off of 500 eV was found to be sufficient to converge the total energy of Au_{38} or Pd_{38} nanoparticles to less than 0.008 eV and so this cut-off was used throughout this study. Since we are modelling isolated nanoparticles only the Γ-point is needed in reciprocal space (*k*-point grid sampling $1 \times 1 \times 1$). All calculations are performed using the generalized gradient approximation (GGA) using the functional of Perdew, Burke and Ernzerhof (PBE) [57]. PW91 was not chosen as a suitable functional as it is widely reported to overestimate the binding energy of small molecules to metal surfaces [58,59]. All calculations are spin unrestricted and the Projector Augmented Wave method (PAW) is used to represent core states [60,61]. For gold this means that there are 60 core electrons represented by PAW and the states for 19 valence electrons are calculated explicitly while Pd has 36 core and 10 valence electrons. As these M_{38} particles differ from bulk metal it is assumed they contain discrete orbital energies as opposed to continuous bands observed within bulk metals therefore Gaussian smearing with a very small width of 0.001 was employed within VASP to ensure electronic smearing does not occur at the Fermi level. All geometry relaxations were performed with electronic and geometric convergence criteria set to 10^{-6} eV and 0.05 eV Å^{-1} respectively. For all geometry relaxation calculations using M_{38} clusters all atoms of adsorbate and clusters were allowed to move to find minima with no atomic restraints applied.

For the periodic slab calculations, 5-layered slabs were created by cleaving the optimised bulk fcc unit cells along the (111) and the (100) surfaces. Supercells in the surface vectors were then created by a (2×2) expansion for the (111) slab and a (3×3) expansion for the (100) case so that the number of atoms in the (111) and (100) slabs was set to 80 and 90 atoms respectively. In order to avoid interactions between the periodically repeated slabs, a vacuum gap of 13 Å was used. The bottom three layers of each slab were fixed at their optimised bulk co-ordinates and the top two layers were free to move during optimisation calculations. The plane wave cut off for slab calculations was set to 400 eV. Slab calculations were carried out using the PBE + D3 level of theory and a

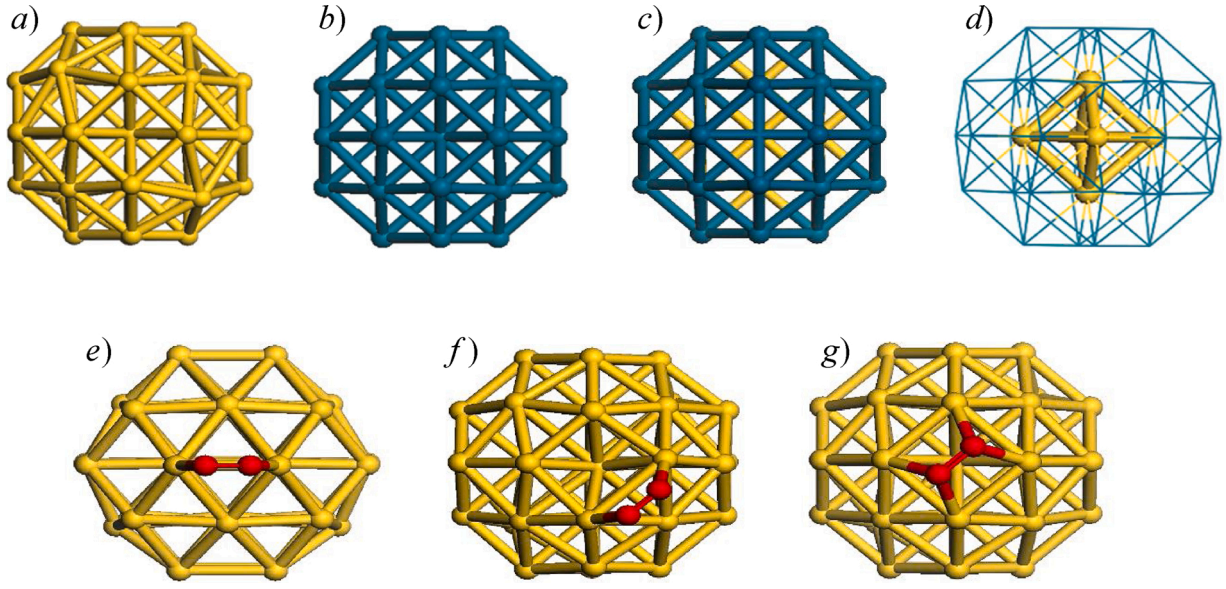

Fig. 1. Structure of M_{38} clusters and molecular adsorption sites, *a*) Au_{38}, *b*) Pd_{38}, *c*) Au_6Pd_{32}, *d*) Au_6Pd_{32}, with Pd atoms shown in wireframe to highlight Au_6 core. optimised structures for molecular adsorption of O_2 on Au_{38} are also shown with O_2(ads) at *e*) the (111)-(111) edge, *f*) the (111)-(100) edge, *g*) the (100) face. Atom colours: Au; yellow, Pd; blue, O; red. (For interpretation of the references to colour in this figure legend, the reader is referred to the web version of this article).

dipole correction along the z-direction of the slab, perpendicular to the exposed surface, was included in all calculations.

The adsorption energy, E_{ads}, for the various molecular species was calculated as:

$$E_{ads} = E_{cl+m} - E_{cl} - E_{m} \quad (9)$$

Where, E_{cl+m}, is the calculated total energy for the optimised cluster or slab with the adsorbate in a given location, E_{cl}, is the calculated total energy for the optimised cluster or slab alone and E_m, is the calculated total energy for the optimised molecule alone, effectively in the gas phase. All three calculations employ the same periodic simulation cell and calculation parameters as defined above.

The research was carried out in two stages, firstly the adsorption and dissociation of dioxygen to Au_{38}, Pd_{38} and a Pd_{32} shell/Au_6 core particle was considered in detail. Then calculations on the reaction of the adsorbed oxygen with dihydrogen and water were carried out. Oxygen adsorption was also used to compare pure PBE and PBE with dispersion corrections (PBE + D3) approaches and then the PBE + D3 approach was used to study the reaction scheme for hydrogen addition to O_2 to produce a surface bound OOH species.

Interaction of O_2 with the metal nanoparticles can lead to charge transfer from O_2 towards the cluster along with back donation from the metal into the π^* orbital of O_2. To assess the balance of these processes, and decide the dominant direction of charge transfer, Bader charge analysis was performed to deduce atomic charges. This method applied to the charge density grid from VASP calculations, and was developed by Henkelman et al. [62–64]. Grid spacing for Bader charge analysis was determined through investigation of a test system in which O_2 was adsorbed onto an Au_{13} cluster. Total charge transfer to/from the O_2 molecule was determined by subtracting the calculated Bader charge from the valence charge of oxygen and the grid density increased until convergence was achieved at a grid spacing of 0.05 Å. The molecular oxygen charges are defined as the sum of excess charge on the two atoms so that a negative value indicates the oxygen molecule has gained electron density, whilst a positive value indicates O_2 has donated electron density to the metal particle.

For the reactions presented here the energy of the transition state was estimated from the structure of the transition state on the minimum energy path between reactants and products using the Nudged Elastic Band (NEB) [65] method usually refined with the with climbing image modification developed by Henkelmen and co-workers [66,67]. The NEB method works by taking the start and end point of a reaction mechanism (the two minima) and interpolating a number of images between them. We use between 5 and 10 images in the NEB calculations to identify the transition states presented here, with the initial interpolation carried out using linear interpolation for diatomic dissociation and a group centred interpolation approach [68] for more complex cases. Transition states were verified by performing a frequency calculation on the proposed transition state system in order to locate a single imaginary frequency mode.

3. Results and discussion

3.1. Adsorption of oxygen

The truncated octahedral structure of the M_{38} particles used in this study is shown in Fig. 1*a*) – *d*). This shape is bounded by 8 hexagonal (111) like facets and 6 square (100) like facets and is one of the low energy structures seen for fcc metals in calculations [69] and used to represent nanoparticles in simulation of reaction pathways [70]. Nanoparticles with mostly (111) and (100) facets are also seen in high resolution STM images [71] of supported metals such as Pd and in high resolution electron microscopy studies of supported Au and Pd catalysts [72]. The compositions used in this study consist of Au_{38} (Fig. 1*a*), Pd_{38} (Fig. 1*b*) and a particle with an Au_6 core and Pd_{32} shell (Fig. 1*c* and *d*). These clusters are around 1 nm in diameter and so represent the smaller end of the experimentally observed particle size distributions. However, they do contain the dominant crystal facets and edge and corner sites that would be expected for the nanoparticles active in direct H_2O_2 synthesis. As computational cost increases rapidly with cluster size these M_{38} clusters also allow the large number of adsorption and barrier calculations carried out in this work to be undertaken. Experimentally, mixed Au and Pd catalysts have the highest activities for direct hydrogen peroxide synthesis and core-shell particles with this arrangement have been noted in electron microscopy studies of active catalysts, [73] although later studies demonstrated that random alloy particles are just as effective [3]. In this modelling study we will use the core shell particle to consider the influence of Au on the reactivity of Pd with adsorbed oxygen. Each nanocluster was cut from the fcc structure of the parent bulk metal with the core shell particle adapted from the Pd_{38} cluster by replacing the central six atoms with Au. Each was then placed in a cubic simulation periodic cell with a side dimension of 25 Å and fully relaxed prior to use with the addition of adsorbates. The resulting energies allow us to estimate the energy of formation of each nanoparticle from the bulk solid giving Au_{38}: 60 kJ mol^{-1}, Pd_{38}: 90 kJ mol^{-1} and Au_6Pd_{38}: 92 kJ mol^{-1}, where the values refer to a mole of atoms in each case. We note that the values are all positive, because of the surfaces created when cutting the clusters from the bulk lattice. Also that the mixed particle has the highest formation, presumably because an additional interface between Au and Pd is introduced. We also find that the average energy per atom to create the mixed metal nanoparticle from the single metal M_{38} structures is only 7 kJ mol^{-1}, suggesting that segregation of the nanoparticles is not as favourable as their agglomeration.

A survey of possible locations for O_2 adsorption on the Au_{38} cluster identified the three geometries shown in Fig. 1*e-g* as the most favourable and these have been selected to compare oxygen adsorption on the clusters studied. For all clusters O_2 adsorption on the (100) face (Fig. 1*g*) gives a structure in which each oxygen atom is in a bridge position, whereas, at the two edge sites, (111)-(111) (Fig. 1*e*) and (111)-(100) (Fig. 1*f*) each O atom co-ordinates to a single M atom of the cluster. Fig. 1*e-g*, actually shows the calculated geometries for the case of Au_{38}. The response of the metal cluster to the presence of the adsorbate can also be seen in these images, for example in Fig. 1*f* adsorption of oxygen at the (111)-(100) edge site causes an increase in the Au-Au spacing for the metal atoms that are coordinated to the molecule.

Table 1 gives a summary of the adsorption energies for each of the molecular species considered in this work. At the PBE level of theory we find that the strongest adsorption for O_2 occurs at the edge formed by the junction of a (111) and (100) face on the Au_{38} cluster, with adsorption to the (100) face 11 kJ mol^{-1} less favourable. This preference is reversed on Pd_{38} and Au_6Pd_{32}, where a much more favourable adsorption energy is found for O_2 directly adsorbed to the (100) facet. Pd_{38} also shows stronger adsorption of molecular oxygen than Au, with the adsorption energies between 52 kJ mol^{-1} and 96 kJ mol^{-1} more negative than for the Au case. The adsorption energy is strengthened further by the introduction of an Au core in the Pd particle with adsorption of O_2 to the (100) facet of the Au_6Pd_{32} particle some 17 kJ mol^{-1} more favourable than seen for the pure Pd nanoparticle. This could be due to the larger Au atoms in the core placing the surface Pd structure under strain [74] or an electronic effect of the Au core on the Pd shell [75].

In all cases, Bader charge analysis shows that oxygen adsorption is accompanied by electron transfer from the metal particle to the molecule. As the partially occupied orbitals of O_2(g) are anti-bonding π^* orbitals this charge transfer is accompanied by an elongation of the O—O bond. Fig. 2 shows the relationship between the charge transfer calculated using Bader analysis and the bond extension compared to O_2(g) in the triplet state calculated at the same level of theory. In all cases the greatest bond extension and charge transfer effects are seen for adsorption to the (100) facet, with the calculated Bader charge for the O_2 adsorbate being between −0.73 $|e|$ on the Pd_{38} and Au_6Pd_{32} clusters and -0.81 $|e|$ on the Au_{38}. This level of charge transfer is consistent with

Table 1
Adsorption energies calculated for molecular adsorption in the three different positions on the clusters studied.

System / method	E_{ads} / kJ mol^{-1} (111)-(111) edge	(111)-(100) edge	(100) face
O_2, Au_{38} / PBE	−65	−69	−58
O_2, Pd_{38} / PBE	−124	−122	−153
O_2, Au_6Pd_{32} / PBE	−139	−142	−170
O_2, $Au_{38}O_2$[a] / PBE	—	—	−8
O_2, $Pd_{38}O_2$[a] / PBE	—	—	−166
O_2, $Au_6Pd_{32}O_2$[a] / PBE	—	—	−174
O_2, Au_{38} / PBE + D3	−70	−93	−74
O_2, Pd_{38} / PBE + D3	−134	−133	−234[b]
H_2, Au_{38} / PBE + D3	−3	−19	−40[b]
H_2, Pd_{38} / PBE + D3	—	−104[b]	−100[b]
H_2O, Au_{38} / PBE + D3	−16	−26	−20
H_2O, Pd_{38} / PBE + D3	−23	−5	−24
H_2, $Au_{38}O_2$(ads) / PBE + D3	−100	−86	−87
H_2, $Pd_{38}O_2$(ads) / PBE + D3	——	−106[b,c]	——
H_2O, $Au_{38}O_2$(ads) / PBE + D3	−134 (111)[d]	——	——

Note: *a*) Molecular adsorption of second O_2 molecule in the presence of 2O(ads) *b*) On optimisation molecule dissociated. *c*) H atoms adsorbed in a bridging motif at the (111)-(100) edges. *d*) Water adsorbed with O at the centre of (111) facet forming H-bond to O_2(ads).

the oxidation of the cluster and formation of a superoxo, O_2^-, surface species. The effect also indicates that, particularly at the (100) location, the molecule is activated toward dissociation. For Pd nanoparticles of similar dimension to those used here, Tian et al. have also observed greater charge transfer to O_2(ads) adsorbed to facets than to edge sites [76].

Calculating the barrier to dissociation for O_2 using the NEB technique requires the identification of atomic adsorption sites for O atoms to use as the end point of the process. The lowest energy adsorption sites for atomic oxygen are in the three fold hollow sites of the (111) facet. Calculations on the atomic adsorption of O were also carried out to identify the lowest energy end points for the dissociation process with the proviso that they are also close enough to the molecular adsorption site to minimise the movement of the O atoms during the bond cleavage. Fig. 3*a* shows the pathways considered, starting from the (111)-(111) edge or (100) facet there is only one choice of end point. However, there were actually three possibilities identified for the end point for an O_2 molecule adsorbed at the (111)-(100) edge. Accordingly five possible oxygen dissociation pathways were used on the Au_{38}, Pd_{38} and Au_6Pd_{32} clusters at the PBE level of theory and the resulting barrier plots shown in Fig. 3*b*.

As has been noted from Table 1, the adsorption of molecular oxygen to the Pd_{38} and Au_6Pd_{32} clusters is notably more favourable than adsorption to the Au_{38} cluster and this is seen again in Fig. 3*b* with all the molecular adsorption geometries for Au_{38} at least 49 kJ mol^{-1} higher in energy than any of the adsorption energies for Pd containing clusters.

On the Au_{38} cluster the highest transition state energies are found for pathways A,D and C with energies relative to Au_{38} + O_2(g) of between 70 and 84 kJ mol^{-1}. The corresponding barrier energies relative to the adsorbed state, ΔE_b, are given in Table 2 and range from 140 to 158 kJ mol^{-1}. This group is followed by route B with a transition state energy 55 kJ mol^{-1} lower in energy. It should be noted that a transition state energy greater than 0 kJ mol^{-1} on these potential energy surfaces, which are relative to gas phase reagents and a clean cluster, implies that desorption of O_2 would have a higher rate than dissociation. Finally for Au_{38} on Fig. 3, route E, starting from the (100) facet adsorption site, gives the lowest transition state energy (−19 kJ mol^{-1}) and barrier (39 kJ mol^{-1}). Inspection of the transition state geometries suggest that the (100) facet provides a particularly favourable route to dissociation, because the O atoms maintain a bridged geometry throughout the dissociation process, whereas for the other routes the transition state has at least one of the O atoms that is only singly co-ordinated to the cluster.

The importance of the (100) site for the dissociation of oxygen over Au clusters has been noted previously in the calculations of Boronat and Corma, [77] Roldan et al. [78] and Staykov et al. [79]. Even though the Au_{38} molecular and atomic adsorption structures are clearly energetically higher than those of the Pd_{38} and the Au_6Pd_{32} core-shell structured clusters the transition state energies are not so clearly delineated. Routes C, A and D on Pd_{38} and B and C on Au_6Pd_{32} actually have higher transition state energies than the lowest TS on Au_{38}, route E. The combination of more favourable adsorption energies for O_2(ads) and these high transition states leads to much higher barriers to molecular dissociation for these routes over the Pd containing particles (Table 2). However, there are lower barriers for the Pd containing systems, in particular route E is also preferred over both Pd_{38} and Au_6Pd_{32}, giving a vanishingly small (< 1 kJ mol^{-1}) barrier on Pd_{38} and a small (12 kJ mol^{-1}) barrier over Au_6Pd_{32}.

These data shows that the activation of O_2(ads) noted from the Bader charge analysis and bond length extension reported in Fig. 2 leads to the facile dissociation of the molecule on Pd_{38} and Au_6Pd_{32} and dissociation with a small barrier over Au_{38}. This occurs *via* adsorption of the molecule to the (100) facet of the clusters, followed by dissociation to produce atomically adsorbed oxygen on the neighbouring (111) faces *via* route E of Fig. 3*a*. This is the first step in the oxidation of the clusters and so suggests that the Pd containing clusters in particular will be prone to oxidation when oxygen is present in the reaction mixture. To explore this further we also looked at the further addition of oxygen to the clusters.

As we have identified route E starting from the (100) facet of the M_{38}

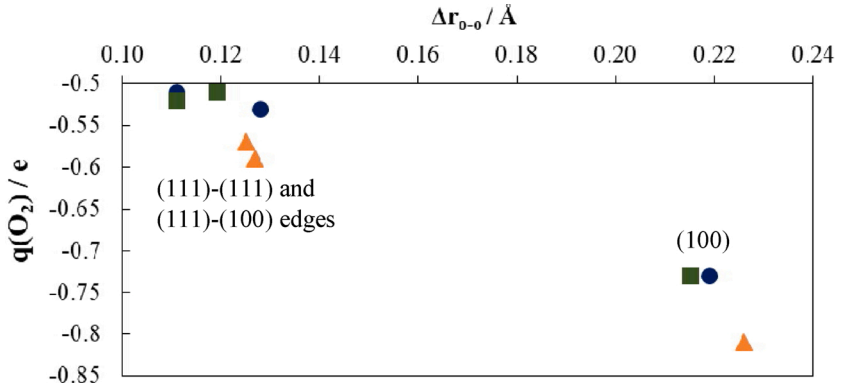

Fig. 2. Relationship between bond extension and charge transfer for O_2(ads) calculated at the PBE level. Au_{38} (Yellow diamonds) Pd_{38} (blue circles) and Au_6Pd_{32} (green squares). Sites at (111)-(111) and (111)-(100) edges and in the (100) face form two distinct groupings as indicated. (For interpretation of the references to colour in this figure legend, the reader is referred to the web version of this article).

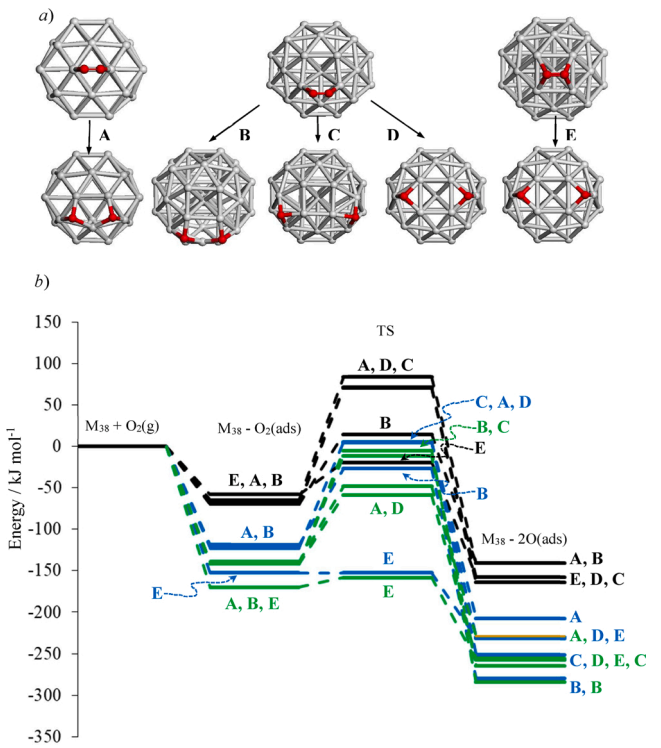

Fig. 3. *a*) Oxygen dissociation pathways considered starting from O_2(ads) at A) (111)-(111) edge, B, C, D) (111)-(100) edge, and E) (100) facet. Pathways end with atomic oxygen in nearest three fold hollow sites. Atom colours; metal, M: grey, O: red. *b*) Calculated potential energy surface for oxygen dissociation following pathways defined in (*a*) with Au_{38} (black), Pd_{38} (blue) and Au_6Pd_{32}(green). Where levels are closely spaced letters are given in highest to lowest order. (For interpretation of the references to colour in this figure legend, the reader is referred to the web version of this article).

Table 2
Calculated barrier energies for O_2 dissociation relative to the molecularly adsorbed state at the PBE level of theory.

	ΔE_b / kJ mol^{-1}		
Route[a] / O_2(ads) site	Au_{38}	Pd_{38}	Au_6Pd_{32}
A / (111)-(111) edge	149	127	91
B / (111)-(100) edge	84	92	137
C / (111)-(100) edge	140	125	130
D / (111)-(100) edge	158	124	83
E / (100) face	39	< 1	12
E / Second O_2(ads)[b]	50	5	8

Note: *a*) As defined in Fig. 3*a*. *b*) Adsorption and dissociation of a second molecule of O_2 on the cluster already having the 2O(ads) from the first adsorption.

clusters as providing the lowest barrier to dissociation in all cases the dissociation of a second molecule of O_2 was also started from the same position. For the second molecule we tested adsorption at all of the (100) facets of the clusters, each cluster has 6 such facets. Fig. 4 shows the potential energy surface for the Au_{38}, Pd_{38} and Au_6Pd_{32} cases with inset images showing the lowest energy starting points. In each case the optimal molecular adsorption is at a different (100) facet to that at which the first O_2 molecule dissociated. This means that the second molecule has available nearby three-fold hollow sites on the adjacent (111) facets to accommodate the dissociated O atoms formed when the bond is broken. The adsorption energies calculated for the second O_2 molecule have also been included in Table 1. For this second adsorption the behaviour of $Au_{38}O_2$ is quite different to that of the Pd containing clusters. The adsorption energy of the second O_2(ads) is 50 kJ mol^{-1} less

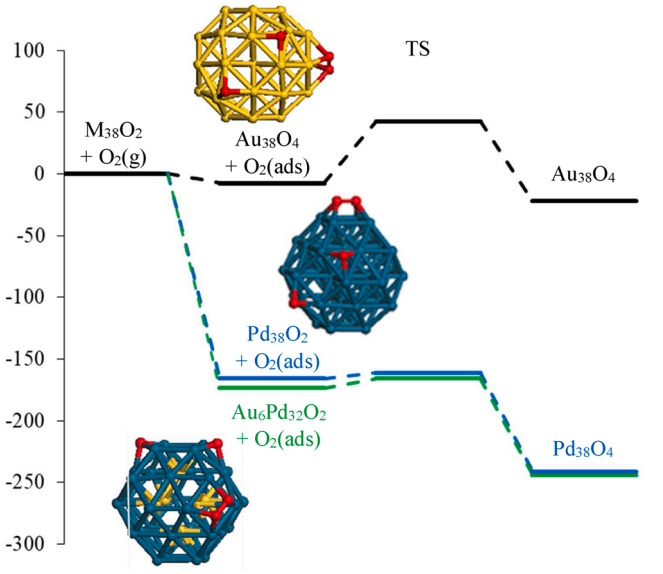

Fig. 4. Calculated potential energy surface (PBE level) for the dissociation of a second O_2(ads) molecule *via* route C (Fig. 3*a*). Line colours follow Au_{38}: black, Pd_{38}: (blue), Au_6Pd_{32}: (green). Inset images show the lowest energy O_2(ads) structure for each nanoparticle showing the position relative to the 2O(ads). Atom colours, Au: yellow, Pd: blue, O: red. (For interpretation of the references to colour in this figure legend, the reader is referred to the web version of this article).

favourable than that of the first molecule to adsorb on the pristine cluster, reducing the adsorption energy to just −8 kJ mol^{-1}. Whereas adsorption of the second molecule is actually more favourable than the first by 13 kJ mol^{-1} for Pd_{38} and by 4 kJ mol^{-1} for Au_6Pd_{32}. It appears that the Au_{38} cluster, once partially oxidised, is unable to take up more oxygen as its ability to donate electron density to adsorbates is depleted. Fig. 4 and Table 2 also show that the barrier to dissociation from the molecularly adsorbed state is also increased compared to that for the first molecule of oxygen that was adsorbed. Again, the greatest effect is seen in the case of Au_{38} for which the barrier to dissociate the molecule (50 kJ mol^{-1}) is considerably greater than the energy required to desorb the molecule back into the gas phase reference state (8 kJ mol^{-1}, Table 1). Whereas, for Pd_{38} a small barrier of 5 kJ mol^{-1} is now present and for Au_6Pd_{32} the barrier is actually lower than seen for the first dissociation event. It can also be seen in Fig. 4 that the energy gained on dissociation of the second O_2 molecule over the Pd containing clusters (Pd_{38}: −75 kJ mol^{-1}, Au_6Pd_{32}: −70 kJ mol^{-1}) is significantly greater than that over Au_{38} (−15 kJ mol^{-1}).

These calculations for the dissociation of a second O_2(ads) reinforce the idea that the oxidation of the Au nanoclusters by molecular oxygen will be limited to much lower levels than the Pd systems. They also indicate that for Au to have this influence as part of an AuPd alloy particle it should be present in the surface layers rather than form a strictly segregated core-shell configuration. We note that in experimental studies hydrogen peroxide is produced in an aqueous solvent and calculation presented later in this paper show that water will interact quite strongly with the negatively charge adsorbed oxygen species. So it is likely that the dissociation barriers presented in Fig. 4 will be altered in a water solvent. However, the conclusion that Au nanoparticles are less readily oxidised than Pd nanoparticles is really based on the much lower energy gain on dissociation of O_2(ads) seen for Au than for Pd and so we would expect that this observation would remain valid even if a water environment were included in the calculation.

As we have mentioned, metal oxide formed during the *in situ* preparation of H_2O_2 may be reduced back to the metal through hydrogen reduction, but this will be at a cost in terms of H_2 selectivity as only water will be formed in the process. Given the similarity in results for

oxygen adsorption and dissociation using Pd_{38} and Au_6Pd_{32} it was decided to only consider the pure metal clusters in the remainder of this study.

Table 1 also gives calculated adsorption energies at the PBE + D3 level for molecular O_2 and the other species we will consider for the transfer of hydrogen to O_2(ads) to form the surface hydrogen peroxy species that is the precursor to hydrogen peroxide. The PBE + D3 level calculations for O_2 give a point of comparison between the functional PBE alone and PBE with dispersion corrections included. Dispersion corrections account for van der Waals attractive interactions due to electron correlation at long distances, which are not accounted for in a gradient corrected local density approximation functional such as PBE. These are long range attractive forces and so the calculated adsorption energies tend to become more favourable when dispersion is included [80]. For Au_{38} this makes the calculated adsorption energies between 5 kJ mol^{-1} and 16 kJ mol^{-1} more negative with PBE + D3 compared to the PBE functional alone. The order of the three sites considered is also changed with the (100) facet now 4 kJ mol^{-1} more favourable than the (111)-(111) edge, whereas with PBE alone the calculations favour the (111)-(111) edge by 7 kJ mol^{-1}. Which may be due to the bridge co-ordination of the atoms in the molecule being stabilised by the dispersion interaction over the single atom-atom interactions of the edge sites. Similar levels of enhanced adsorption energies are seen when the PBE + D3 and PBE level calculations are compared for the Pd_{38} nanocluster. However, for the (100) facet a more dramatic effect is seen with the reported energy for PBE + D3, 81 kJ mol^{-1} lower than the end point of the optimisation using PBE alone. Inspection of the end point of this PBE + D3 optimisation showed that the molecule had actually dissociated (O…O distance 2.817 Å) to give two bridge site O atoms. Comparing the adsorption energy for this structure from Table 1 with the PBE end point energy for dissociation *via* route E (Fig. 3) shows that the dispersion corrected energy is 2 kJ mol^{-1} more stable than the PBE value for the two oxygen atoms in the three fold sites of the adjacent (111) surfaces. The dissociation of molecular oxygen at the (100) facet with no barrier in the PBE + D3 calculation may have been expected given the very low barrier calculated at the PBE level (Table 2).

To form an impression of the effect of particle size on the adsorption of oxygen we have also carried out calculations using a slab model to represent the extended (111) and (100) surfaces of much larger particles. Table 3 summarises the calculated molecular oxygen adsorption energies obtained from our slab calculations on extended surfaces using the PBE + D3 approach. For Au(111) no stable O_2(ads) structures were found, which was also the case if O_2 was placed directly over the (111) facet of Au_{38} so that the only sites involving the (111) facet that can adsorb molecular oxygen are the edge sites. For the slab model of Au (100) an analogous geometry to the structure found on the Au_{38} (100) facet was obtained, but on the extended surface the calculated adsorption energy is 34 kJ mol^{-1} less favourable.

For the slab model of Pd(111) favourable adsorption is observed both for a top-top and top-bridge arrangement of the molecule. However, the adsorption energies for the slab calculations are around 30 kJ mol^{-1} less favourable than seen for the edge sites involving the (111) facet for Pd_{38} (Table 1), which demonstrates a preference for oxygen adsorption at the edges of small nanoparticles over the extended close packed facets of larger particles.

On the Pd(100) slab model, the O—O bond remains intact on optimisation of the adsorbed state (O..O = 1.433 Å), indicating that the spontaneous dissociation of O_2(ads) on the Pd_{38} (100) facet of the cluster is a feature of its small size and that even on the more open (100) surfaces of larger particles oxygen dissociation is an activated process.

Table 3
Calculated adsorption energies for O_2 on periodic slab models of the (111) and (100) surfaces of Au and Pd at the PBE + D3 level of theory.

	E_{ads} / kJ mol^{-1}	
Surface / O_2(ads) site	Au	Pd
(111) / top-top[a]	——[b]	−96
(111) / top-bridge[a]	——[b]	−100
(100) / bridge-bridge[a]	−36	−171

Note: *a*) Site defined by the co-ordination of the O atoms in the molecule to surface metal atoms, top: a single O—M bond, bridge: O atom bonded to two surface M atoms. *b*) "—— "indicates that no stable adsorption was found on optimisation of the system.

3.2. Adsorption of H_2 and H_2O and their reaction with O_2(ads)

Table 1 also lists the calculated adsorption energies for H_2 and H_2O on the Au_{38} and Pd_{38} cluster models using the PBE + D3 level of theory both on the pristine cluster and on the cluster with O_2(ads) pre-adsorbed at the (111)-(100) edge. This position was chosen as the lowest energy site for O_2 adsorption on the Au_{38} cluster and was also used for all calculations on the reaction of O_2(ads) with co-adsorbates for Au_{38} and Pd_{38}. For Pd_{38} the (100) facet was preferred over this edge site but at the PBE + D3 level the molecule dissociated and adsorption at this position would not be suited to H_2O_2 synthesis. For the pristine Au_{38} nanoparticle adsorption of a H_2 molecule on either of the edge sites optimises to give a structure with the H—H bond intact. Although, the molecule tends to migrate to interact with a single metal atom of the cluster within the designated site. The resulting adsorption energies for H_2 in the molecular state on Au_{38} are much lower in magnitude than found for O_2 with the most favourable only −19 kJ mol^{-1} compared with −93 kJ mol^{-1} for O_2 at the same (111)-(100) edge site. On the (100) facet of the Au_{38} cluster, H_2 does dissociate, but in this case the adsorption energy of dissociated H_2 is only −40 kJ mol^{-1} relative to the molecule in the gas phase and the isolated cluster. For the clean Pd_{38} cluster H_2 is dissociated when adsorbed at any of the sites tested and gives much more favourable adsorption energies.

The potential energy diagram for the reaction of adsorbed hydrogen with O_2(ads) to form a surface bound hydroperoxyl species is shown in Fig. 5. The potential energy surface is referenced to the pristine cluster and the gas phase reagents, O_2(g) and H_2(g) and it is notable in all cases that the change of energy seen in the initial step, which represents the co-adsorption of the reagents, is much greater than would be expected from the sum of the adsorption energies for O_2 and H_2 onto the pristine clusters given in Table 1. To quantify this further Table 1 also gives the

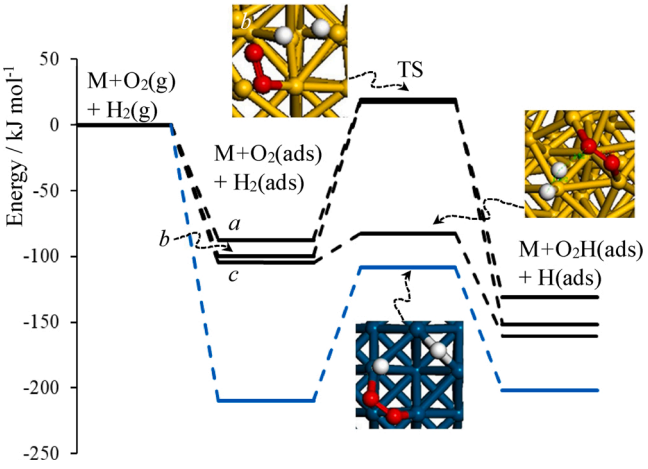

Fig. 5. The calculated potential energy surface for the reaction of adsorbed O_2 and H_2 to form a surface OOH peroxy group and atomically adsorbed H. In all cases O_2 is initially at the (111)-(100) site and reacts on Au_{38} with H_2 at *a*) the (111)-(111) site, *b*) the (100) site, and *c*) the (111)-(100) across the (100) facet from the O_2 site, TS images as inserts. The blue trace shows the energy surface for formation of OOH on the Pd_{38} cluster with O_2 initially at (111)-(100) site and atomically adsorbed H. (For interpretation of the references to colour in this figure legend, the reader is referred to the web version of this article).

calculated adsorption energy for H_2 relative to the clusters with O_2(ads) already present. For the edge sites of Au_{38} these values are 97 kJ mol^{-1} ((111)-(111)) and 67 kJ mol^{-1} ((111)-(100)) more favourable than for H_2 adsorbing to the clean nanoparticle at the same positions. On the (100) facet of the clean Au_{38} cluster hydrogen is dissociated on adsorption. However when O_2 is pre-adsorbed at the (111)-(100) edge, dissociation of H_2 does not happen when the H_2 molecule is placed at the (100) facet of the edge, but its adsorption energy in this position is still significantly enhanced. For Pd_{38} the atomically adsorbed H atoms are also slightly stabilised but by only 2 kJ mol^{-1}. We have seen that O_2(ads) is bound to the cluster with a partial charge transfer to the molecule to create a superoxo like species (O_2^-), which means that the particle loses around 1 electron to the oxygen adsorbate and so is slightly oxidised. This electron transfer appears to increase the affinity, particularly of the Au_{38} cluster, for the adsorption of H_2 as it now has the capacity to receive some electron density from this reducing agent. Correspondingly, the adsorption energy of the H_2 molecule is enhanced when the molecule is co-adsorbed with O_2. For the hydrogen peroxide synthesis reaction this observation is informative as it suggests that hydrogen will preferentially adsorb on particles that are partially oxidised.

Following the reaction pathways shown in Fig. 5 for the Au_{38} nanocluster reaction starting from H_2(ads) at the (111)-(111) edge or in the (100) facet results in barriers of 107 kJ mol^{-1} and 118 kJ mol^{-1}, respectively, which are significantly higher than the co-adsorption energy suggesting that, for these routes, H_2 is more likely to desorb than to react. A low energy pathway is identified for H_2 initially adsorbed on the (111)-(100) edge with a transition state energy relative to gas phase reagents of −83 kJ mol^{-1} and a barrier of only 22 kJ mol^{-1}. In this case the H_2 bond is broken as the OOH species is formed. As the O_2(ads) species is actually negatively charged (Fig. 2) it is likely that this hydrogen cleavage is heterolytic in nature, as has been recently suggested for H_2 activation at the Au/TiO_2 interface during the undesired oxidation of hydrogen in the PROX reaction [81].

For Pd_{38} we have noted that H_2 is always dissociated on adsorption and so the potential energy surface for atomically adsorbed H is compared to the Au_{38} routes in Fig. 5. Here there is a significant barrier to reaction from the co-adsorbed state (101 kJ mol^{-1}), although the strength of co-adsorption means that the transition state is still well below the reference state.

Fig. 6 gives the potential energy surfaces for the production of a surface hydroperoxyl species through the reaction of O_2(ads) with water rather than hydrogen, *i.e.* a proton transfer reaction (step 6) rather than a hydrogenation (step 3). For Au_{38} with O_2(ads) pre-adsorbed at the (111)-(100) edge site, water adsorbs strongly on the (111) facet that is involved in the step with an adsorption energy of −134 kJ mol^{-1}, which is 108 kJ mol^{-1} more favourable than any of the sites considered for the clean Au_{38} nanoparticle. The interaction of the oxygen atom of water will be enhanced by the partial oxidation of the cluster but from the structure shown as an inset in Fig. 6 it can also be seen that the adsorption of the water molecule is further stabilised by a hydrogen bond to the superoxo (O_2^-) on the surface. The barrier to proton transfer between water and the adsorbed oxygen molecule is below the energy to desorb the surface species but the barrier for this elementary step is still significant at 107 kJ mol^{-1}. In the transition state as the proton is passed across the (111) facet, it is not stabilised by interactions with oxygen or the surface. As water forms part of the water-methanol solvent used experimentally we also considered proton transfer through a network of H-bonds by introducing a second molecule of water. This forms a hydrogen bonding chain between adsorbed water and the surface superoxo (O_2^-) species. Now in the transition state the proton transfer is stabilised throughout and the barrier is reduced to only 18 kJ mol^{-1}. Finally, the same process was tested for the Pd_{38} cluster giving a protonation barrier when two waters are co-adsorbed with O_2(ads) of 34 kJ mol^{-1}.

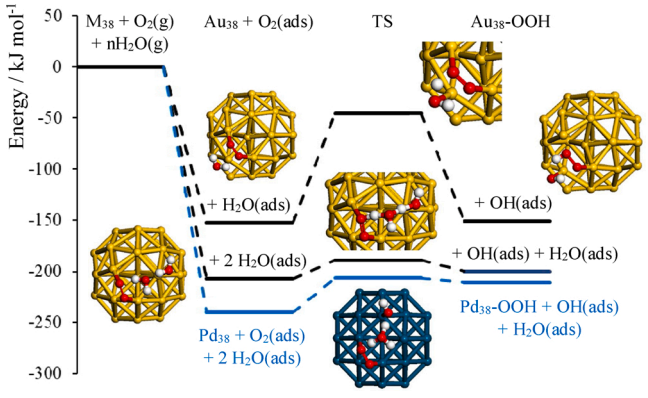

Fig. 6. Calculated potential energy surface (PBE + D3 level) for the protonation of O_2(ads) from co-adsorbed water. Line colours follow Au_{38}: black, Pd_{38}: (blue). Inset images show the calculated structures. Atom colours, Au: yellow, Pd: blue, O: red. (For interpretation of the references to colour in this figure legend, the reader is referred to the web version of this article).

4. Conclusions

We have presented a series of calculations based on Au_{38}, Pd_{38} and an Au_6Pd_{32} core-shell structure relating to their use in the direct conversion of H_2 and O_2 to a surface hydroperoxy species as a precursor to H_2O_2. Firstly the electronic state of O_2(ads) was analysed using Bader charge analysis and it was found that charge donation from the metal clusters to the adsorbate results in a surface superoxide (O_2^-) being formed, and correspondingly partial oxidation of the clusters. This adsorbate is activated toward dissociation showing elongation of the O_2 bond compared to the gas phase reference calculation, particularly when located on the (100) facet. At the PBE level of theory we were able to confirm that there are low energy pathways for the dissociation of O_2(ads) for all three clusters and that for Pd_{38} the barrier is extremely small (< 1 kJ mol^{-1}). However, adsorption and dissociation of a second molecule of O_2 to the $Au_{38}O_2$ cluster was found to be unfavourable with a significant barrier and a transition state higher than the desorption energy for the second molecule, which on the Pd containing clusters was not the case and a second O_2 dissociation event gave a significant lowering of the system energy *via* barriers of less than 10 kJ mol^{-1}. We conclude that deep oxidation of the Pd clusters is much easier than the pure Au case so that in Pd catalysts hydrogen will be used in a side reaction to reduce the metal oxide producing only water. One role of Au will be to limit the oxidation of the catalyst particles, but in our calculations the strict core-shell structure did not show this effect, suggesting that surface Au is required. Indeed, recent work by Tian et al. looking at the addition of Te to Pd nanocluster catalysts for direct synthesis of H_2O_2 observed improved selectivity for Te doped catalysts compared to pure Pd. They were able to use DFT calculations to demonstrate that surface Te helps prevent O_2 dissociation [82].

In the work presented here, oxygen adsorption was also used to compare results from PBE and PBE + D3 levels of theory. As expected the adsorption energies calculated became more favourable when dispersion corrections are included and there was also a knock-on effect that dissociation of O_2(ads) at the Pd_{38} (100) facet became spontaneous so that the small barrier observed at the PBE level was eliminated.

The co-adsorption of hydrogen or water on Au_{38} or Pd_{38} using the PBE + D3 approach was found to be more favourable with O_2(ads) present than for the pristine nanoparticles, which can be understood from the charge transfer information obtained in our analysis of oxygen adsorption. The partial oxidation of the cluster will increase its affinity for electron donation from H_2 and from the lone pair of the oxygen atom of water. In addition the superoxo (O_2^-) state of O_2(ads) can be involved in hydrogen bonding with water.

The hydrogenation of O_2(ads) from co-adsorbed hydrogen was found to have low energy pathways for Au_{38} (ΔE_b =22 kJ mol^{-1}) and for Pd_{38}

the route considered has a barrier considerably lower than the co-adsorbed state (E_{ads} = −210 kJ mol^{-1}, ΔE_b =101 kJ mol^{-1}), which would suggest the hydroperoxy species can be readily formed by this route over Au catalysts but that the rate should be slower over pure Pd nanoparticles. Although, we note that the number of co-adsorbed structures has not been completely explored in this case.

The protonation of O_2(ads) from water was found to follow a low energy route for both metals; Au_{38} (ΔE_b =18 kJ mol^{-1}) and Pd_{38} (ΔE_b =34 kJ mol^{-1}) provided a proton shuttle could be set up using two water molecules. Clearly the model using only two waters in this stage of the mechanism may not capture the full effect of the aqueous solvent used experimentally and we intend to extend these calculations to include further solvation shells and consider the free energy barriers to reaction protonation using a dynamics approach. Even so, the current work shows that protonation from solvent molecules presents a reaction pathway with barriers at least as low as the direct hydrogenation from H_2.

To return to the question of the preferred mechanism for hydrogen peroxide synthesis it is useful to consider the experimental conditions that are usually employed [43,73]. Typically the reaction is run at elevated pressure with 2.9 MPa H_2 (5 % volume fraction)/CO_2 and 1.1 MPa O_2 (25 % volume fraction)/CO_2, to give partial pressures of 0.145 MPa H_2 and 0.275 MPa O_2 in the head space over a solvent volume formed from 5.6 g methanol and 2.9 g water, around 9.4 cm^3. Assuming that the Henry's constant of H_2 in water [50] (7.7 × 10^{-6} mol m^{-3} Pa^{-1}) is applicable to this mixture we estimate a solution concentration of [H_2] = 2.2 × 10^{-5} mol cm^{-3}. From the solvent composition, the concentration of water is effectively [H_2O] = 1.7 × 10^{-2} mol cm^{-3}. Given that the calculated energetics suggest that either route is possible, in practice the protonation of O_2(ads) to form hydrogen peroxide followed by the reduction of the resulting oxidised particle by H_2 is likely to be the dominant route.

This work also suggests that the incorporation of molecular oxygen into reactions that usually employ hydrogen peroxide is best achieved when O_2 is activated on the nanoparticles themselves rather than at the interface with an oxide support, where dissociation is more likely [16].

CRediT authorship contribution statement

Nishtha Agarwal: Data curation, Formal analysis. **Liam Thomas:** Data curation, Formal analysis. **Ali Nasrallah:** Data curation, Formal analysis, Writing - review & editing. **Mala A. Sainna:** Data curation, Formal analysis, Writing - review & editing. **Simon J. Freakley:** Validation, Writing - review & editing. **Jennifer K. Edwards:** Validation, Writing - review & editing. **C. Richard A. Catlow:** Conceptualization, Writing - review & editing, Funding acquisition. **Graham J. Hutchings:** Conceptualization, Writing - review & editing, Funding acquisition. **Stuart H. Taylor:** Writing - review & editing, Funding acquisition. **David J. Willock:** Conceptualization, Writing - original draft, Funding acquisition.

Declaration of Competing Interest

The authors declare that they have no known competing financial interests or personal relationships that could have appeared to influence the work reported in this paper.

Acknowledgements

We would like to thank the Engineering and Physical Sciences Reasearch Council (EPSRC) for funding this work (Grant reference codes: EP/P033695/1 and EP/L027240/1). *via* our membership of the UK's HEC Materials Chemistry Consortium, which is funded by EPSRC (EP/L000202, EP/R029431), this work used the ARCHER UK National Supercomputing Service (http://www.archer.ac.uk) and the UK Materials and Molecular Modelling Hub for computational resources, MMM Hub, which is partially funded by EPSRC (EP/P020194). Information on the data underpinning the results presented here, including how to access them, can be found in the Cardiff University data catalogue at http://doi.org/10.17035/d.2020.0116559060.

References

[1] T. Ishida, T. Murayama, A. Taketoshi, M. Haruta, Importance of size and contact structure of gold nanoparticles for the genesis of unique catalytic processes, Chem. Rev. 120 (2020) 464–525.
[2] A.S.K. Hashmi, G.J. Hutchings, Gold catalysis, Angew. Chem. Int. Ed. 45 (2006) 7896–7936.
[3] J.K. Edwards, S.J. Freakley, A.F. Carley, C.J. Kiely, G.J. Hutchings, Strategies for designing supported gold–palladium bimetallic catalysts for the direct synthesis of hydrogen peroxide, Acc. Chem. Res. 47 (2014) 845–854.
[4] A. Villa, S.J. Freakley, M. Schiavoni, J.K. Edwards, C. Hammond, G.M. Veith, W. Wang, D. Wang, L. Prati, N. Dimitratos, G.J. Hutchings, Depressing the hydrogenation and decomposition reaction in H_2 O_2 synthesis by supporting AuPd on oxygen functionalized carbon nanofibers, Catal. Sci. Technol. 6 (2016) 694–697.
[5] M. Haruta, T. Kobayashi, H. Sano, N. Yamada, Novel gold catalysts for the oxidation of carbon-monoxide at a temperature far below 0-Degree-C, Chem. Lett. (1987) 405–408.
[6] M. Haruta, Spiers Memorial Lecture Role of perimeter interfaces in catalysis by gold nanoparticles, Faraday Discuss. 152 (2011) 11–32.
[7] B.T. Qiao, J.X. Liu, Y.G. Wang, Q.Q. Lin, X.Y. Liu, A.Q. Wang, J. Li, T. Zhang, J. Y. Liu, Highly efficient catalysis of preferential oxidation of CO in H-2-Rich stream by gold single-atom catalysts, ACS Catal. 5 (2015) 6249–6254.
[8] N. Lopez, J.K. Nørskov, Catalytic CO oxidation by a gold nanoparticle: a density functional study, J. Am. Chem. Soc. 124 (2002) 11262–11263.
[9] M. Valden, Onset of catalytic activity of gold clusters on Titania with the appearance of nonmetallic properties, Science 281 (1998) 1647–1650.
[10] A. Sanchez, S. Abbet, U. Heiz, W.-D. Schneider, H. Häkkinen, R.N. Barnett, U. Landman, When gold is not noble: nanoscale gold catalysts, J. Phys. Chem. A 103 (1999) 9573–9578.
[11] B. Yoon, H. Häkkinen, U. Landman, A.S. Wörz, J.-M. Antonietti, S. Abbet, K. Judai, U. Heiz, Charging effects on bonding and catalyzed oxidation of CO on Au8 clusters on MgO, Science 307 (2005) 403–407.
[12] J. Xu, T. White, P. Li, C. He, J. Yu, W. Yuan, Y.-F. Han, Biphasic Pd−Au alloy catalyst for low-temperature CO oxidation, J. Am. Chem. Soc. 132 (2010) 10398–10406.
[13] Y.Y. Wu, N.A. Mashayekhi, H.H. Kung, Au–metal oxide support interface as catalytic active sites, Catal. Sci. Technol. 3 (2013) 2881.
[14] D. Widmann, R.J. Behm, Activation of molecular oxygen and the nature of the active oxygen species for CO oxidation on oxide supported Au catalysts, Acc. Chem. Res. 47 (2014) 740–749.
[15] A.A. Herzing, C.J. Kiely, A.F. Carley, P. Landon, G.J. Hutchings, Identification of active gold nanoclusters on iron oxide supports for CO oxidation, Science 321 (2008) 1331–1335.
[16] K.L. Howard, D.J. Willock, A periodic DFT study of the activation of O2 by Au nanoparticles on α-Fe2O3, Faraday Discuss. 152 (2011) 135.
[17] S. Chen, L. Luo, Z. Jiang, W. Huang, Size-dependent reaction pathways of low-temperature CO oxidation on Au/CeO_2 catalysts, ACS Catal. 5 (2015) 1653–1662.
[18] M.A. Saqlain, A. Hussain, M. Siddiq, A.A. Leitão, A DFT+U study of the Mars Van Krevelen mechanism of CO oxidation on Au/TiO2 catalysts, Appl. Catal. Gen. 519 (2016) 27–33.
[19] D. Widmann, A. Krautsieder, P. Walter, A. Brückner, R.J. Behm, How temperature affects the mechanism of CO oxidation on Au/TiO_2: a combined EPR and TAP reactor study of the reactive removal of TiO $_2$ surface lattice oxygen in Au/TiO $_2$ by CO, ACS Catal. 6 (2016) 5005–5011.
[20] I.X. Green, W. Tang, M. Neurock, J.T. Yates, Insights into catalytic oxidation at the Au/TiO_2 dual perimeter sites, Acc. Chem. Res. 47 (2014) 805–815.
[21] M. Sankar, Q. He, R.V. Engel, M.A. Sainna, A.J. Logsdail, A. Roldan, D.J. Willock, N. Agarwal, C.J. Kiely, G.J. Hutchings, Role of the support in gold-containing nanoparticles as heterogeneous catalysts, Chem. Rev. (2020) acs.chemrev.9b00662.
[22] S. Biella, Gold catalyzed oxidation of aldehydes in liquid phase, J. Mol. Catal. Chem. 197 (2003) 207–212.
[23] H. Tsunoyama, H. Sakurai, Y. Negishi, T. Tsukuda, Size-specific catalytic activity of polymer-stabilized gold nanoclusters for aerobic alcohol oxidation in water, J. Am. Chem. Soc. 127 (2005) 9374–9375.
[24] K. Mori, T. Hara, T. Mizugaki, K. Ebitani, K. Kaneda, Hydroxyapatite-supported palladium nanoclusters: a highly active heterogeneous catalyst for selective oxidation of alcohols by use of molecular oxygen, J. Am. Chem. Soc. 126 (2004) 10657–10666.
[25] S. Biella, M. Rossi, Gas phase oxidation of alcohols to aldehydes or ketones catalysed by supported gold, Chem. Commun. (2003) 378–379.
[26] B.N. Zope, D.D. Hibbitts, M. Neurock, R.J. Davis, Reactivity of the gold/water interface during selective oxidation catalysis, Science 330 (2010) 74–78.
[27] D.I. Enache, J.K. Edwards, P. Landon, B. Solsona-Espriu, A.F. Carley, A.A. Herzing, M. Watanabe, C.J. Kiely, D.W. Knight, G.J. Hutchings, Solvent-free oxidation of primary alcohols to aldehydes using Au-Pd/TiO_2 catalysts, Science 311 (2006) 362–365.

[28] M.D. Hughes, Y.-J. Xu, P. Jenkins, P. McMorn, P. Landon, D.I. Enache, A.F. Carley, G.A. Attard, G.J. Hutchings, F. King, E.H. Stitt, P. Johnston, K. Griffin, C.J. Kiely, Tunable gold catalysts for selective hydrocarbon oxidation under mild conditions, Nature 437 (2005) 1132–1135.
[29] H. Alshammari, P.J. Miedziak, T.E. Davies, D.J. Willock, D.W. Knight, G. J. Hutchings, Initiator-free hydrocarbon oxidation using supported gold nanoparticles, Catal. Sci. Technol. 4 (2014) 908–911.
[30] H. Alshammari, P.J. Miedziak, D.W. Knight, D.J. Willock, G.J. Hutchings, The effect of ring size on the selective oxidation of cycloalkenes using supported metal catalysts, Catal. Sci. Technol. 3 (2013) 1531.
[31] T. Hayashi, K. Tanaka, M. Haruta, Selective vapor-phase epoxidation of propylene over Au/TiO_2 catalysts in the presence of oxygen and hydrogen, J. Catal. 178 (1998) 566–575.
[32] X. Lu, G. Zhao, Y. Lu, Propylene epoxidation with O2 and H2: a high-performance Au/TS-1 catalyst prepared via a deposition–precipitation method using urea, Catal. Sci. Technol. 3 (2013) 2906.
[33] A. Prieto, M. Palomino, U. Díaz, A. Corma, One-pot two-step process for direct propylene oxide production catalyzed by bi-functional Pd(Au)@TS-1 materials, Appl. Catal. Gen. 523 (2016) 73–84.
[34] M.H. Ab Rahim, M.M. Forde, R.L. Jenkins, C. Hammond, Q. He, N. Dimitratos, J. A. Lopez-Sanchez, A.F. Carley, S.H. Taylor, D.J. Willock, D.M. Murphy, C.J. Kiely, G.J. Hutchings, Oxidation of methane to methanol with hydrogen peroxide using supported gold-palladium alloy nanoparticles, Angew. Chem. Int. Ed. 52 (2013) 1280–1284.
[35] C. Williams, J.H. Carter, N.F. Dummer, Y.K. Chow, D.J. Morgan, S. Yacob, P. Serna, D.J. Willock, R.J. Meyer, S.H. Taylor, G.J. Hutchings, Selective oxidation of methane to methanol using supported AuPd catalysts prepared by stabilizer-free sol-immobilization, ACS Catal. 8 (2018) 2567–2576.
[36] N. Agarwal, S.J. Freakley, R.U. McVicker, S.M. Althahban, N. Dimitratos, Q. He, D. J. Morgan, R.L. Jenkins, D.J. Willock, S.H. Taylor, C.J. Kiely, G.J. Hutchings, Aqueous Au-Pd colloids catalyze selective CH_4 oxidation to CH_3 OH with O_2 under mild conditions, Science 358 (2017) 223–227.
[37] P. Landon, P.J. Collier, A.F. Carley, D. Chadwick, A.J. Papworth, A. Burrows, C. J. Kiely, G.J. Hutchings, Direct synthesis of hydrogen peroxide from H2 and O2 using Pd and Au catalysts, Phys. Chem. Chem. Phys. 5 (2003) 1917–1923.
[38] P. Landon, P.J. Collier, A.J. Papworth, C.J. Kiely, G.J. Hutchings, Direct formation of hydrogen peroxide from H2/O2 using a gold catalyst, Chem. Commun. (2002) 2058–2059.
[39] J.K. Edwards, B. Solsona, P. Landon, A.F. Carley, A. Herzing, M. Watanabe, C. J. Kiely, G.J. Hutchings, Direct synthesis of hydrogen peroxide from H2 and O2 using Au–Pd/Fe2O3 catalysts, J. Mater. Chem. 15 (2005) 4595.
[40] J.M. Campos-Martin, G. Blanco-Brieva, J.L.G. Fierro, Hydrogen peroxide synthesis: an outlook beyond the anthraquinone process, Angew. Chem. Int. Ed. 45 (2006) 6962–6984.
[41] J. García-Serna, T. Moreno, P. Biasi, M.J. Cocero, J.-P. Mikkola, T.O. Salmi, Engineering in direct synthesis of hydrogen peroxide: targets, reactors and guidelines for operational conditions, Green Chem. 16 (2014) 2320.
[42] A. Plauck, E.E. Stangland, J.A. Dumesic, M. Mavrikakis, Active sites and mechanisms for H_2 O_2 decomposition over Pd catalysts, Proc. Natl. Acad. Sci. 113 (2016) E1973–E1982.
[43] J.K. Edwards, B. Solsona, E. N. N, A.F. Carley, A.A. Herzing, C.J. Kiely, G. J. Hutchings, Switching off hydrogen peroxide hydrogenation in the direct synthesis process, Science 323 (2009) 1037–1041.
[44] D.P. Dissanayake, J.H. Lunsford, Evidence for the role of colloidal palladium in the catalytic formation of H2O2 from H2 and O2, J. Catal. 206 (2002) 173–176.
[45] S. Chinta, A mechanistic study of H2O2 and H2O formation from H2 andBO2 catalyzed by palladium in an aqueous medium, J. Catal. 225 (2004) 249–255.
[46] Q. Liu, K.K. Gath, J.C. Bauer, R.E. Schaak, J.H. Lunsford, The active phase in the direct synthesis of H2O2 from H2 and O2 over Pd/SiO2 catalyst in a H2SO4/ ethanol system, Catal. Lett. 132 (2009) 342–348.
[47] E. Ntainjua N, J.K. Edwards, A.F. Carley, J.A. Lopez-Sanchez, J.A. Moulijn, A. A. Herzing, C.J. Kiely, G.J. Hutchings, The role of the support in achieving high selectivity in the direct formation of hydrogen peroxide, Green Chem. 10 (2008) 1162.
[48] E. Ntainjua N, M. Piccinini, J.C. Pritchard, J.K. Edwards, A.F. Carley, J.A. Moulijn, G.J. Hutchings, Effect of halide and acid additives on the direct synthesis of hydrogen peroxide using supported gold-palladium catalysts, ChemSusChem 2 (2009) 575–580.
[49] J. Pritchard, L. Kesavan, M. Piccinini, Q. He, R. Tiruvalam, N. Dimitratos, J. A. Lopez-Sanchez, A.F. Carley, J.K. Edwards, C.J. Kiely, G.J. Hutchings, Direct synthesis of hydrogen peroxide and benzyl alcohol oxidation using Au−Pd catalysts prepared by sol immobilization, Langmuir 26 (2010) 16568–16577.
[50] R. Sander, Compilation of Henry's law constants (version 4.0) for water as solvent, Atmospheric Chem. Phys. 15 (2015) 4399–4981.
[51] D.W. Flaherty, Direct synthesis of H_2 O_2 from H_2 and O_2 on Pd catalysts: current understanding, outstanding questions, and research needs, ACS Catal. 8 (2018) 1520–1527.
[52] N.M. Wilson, D.W. Flaherty, Mechanism for the direct synthesis of H_2 O_2 on Pd clusters: heterolytic reaction pathways at the liquid–solid interface, J. Am. Chem. Soc. 138 (2016) 574–586.
[53] G. Kresse, J. Hafner, Ab initio molecular dynamics for liquid metals, Phys. Rev. B 47 (1993) 558–561.
[54] G. Kresse, J. Hafner, Ab initio molecular-dynamics simulation of the liquid-metal–amorphous-semiconductor transition in germanium, Phys. Rev. B 49 (1994) 14251–14269.
[55] G. Kresse, J. Furthmüller, Efficiency of ab-initio total energy calculations for metals and semiconductors using a plane-wave basis set, Comput. Mater. Sci. 6 (1996) 15–50.
[56] G. Kresse, Efficient iterative schemes for ab initio total-energy calculations using a plane-wave basis set, Phys. Rev. B 54 (1996) 11169–11186.
[57] J.P. Perdew, K. Burke, M. Ernzerhof, Generalized gradient approximation made simple, Phys. Rev. Lett. 77 (1996) 3865–3868.
[58] T. Visart de Bocarmé, T.-D. Chau, F. Tielens, J. Andrés, P. Gaspard, R.L.C. Wang, H. J. Kreuzer, N. Kruse, Oxygen adsorption on gold nanofacets and model clusters, J. Chem. Phys. 125 (2006), 054703.
[59] Z. Duan, G. Henkelman, CO Oxidation on the Pd(111) Surface, ACS Catal. 4 (2014) 3435–3443.
[60] P.E. Blöchl, Projector augmented-wave method, Phys. Rev. B 50 (1994) 17953–17979.
[61] G. Kresse, From ultrasoft pseudopotentials to the projector augmented-wave method, Phys. Rev. B 59 (1999) 1758–1775.
[62] W. Tang, E. Sanville, G. Henkelman, A grid-based Bader analysis algorithm without lattice bias, J. Phys. Condens. Matter Inst. Phys. J. 21 (2009), 084204.
[63] E. Sanville, S.D. Kenny, R. Smith, G. Henkelman, Improved grid-based algorithm for Bader charge allocation, J. Comput. Chem. 28 (2007) 899–908.
[64] G. Henkelman, A. Arnaldsson, H. Jónsson, A fast and robust algorithm for Bader decomposition of charge density, Comput. Mater. Sci. 36 (2006) 354–360.
[65] G. Mills, H. Jónsson, G.K. Schenter, Reversible work transition state theory: application to dissociative adsorption of hydrogen, Surf. Sci. 324 (1995) 305–337.
[66] G. Henkelman, H. Jónsson, A dimer method for finding saddle points on high dimensional potential surfaces using only first derivatives, J. Chem. Phys. 111 (1999) 7010–7022.
[67] J. Kästner, P. Sherwood, Superlinearly converging dimer method for transition state search, J. Chem. Phys. 128 (2008), 014106.
[68] A. Thetford, G.J. Hutchings, S.H. Taylor, D.J. Willock, The decomposition of H_2O_2 over the components of Au/TiO_2 catalysts, Proc. R. Soc. Math. Phys. Eng. Sci. 467 (2011) 1885–1899.
[69] F. Pittaway, L.O. Paz-Borbón, R.L. Johnston, H. Arslan, R. Ferrando, C. Mottet, G. Barcaro, A. Fortunelli, Theoretical studies of palladium−gold nanoclusters: Pd−Au clusters with up to 50 atoms, J. Phys. Chem. C 113 (2009) 9141–9152.
[70] M. Boronat, S. Laursen, A. Leyva-Pérez, J. Oliver-Meseguer, D. Combita, A. Corma, Partially oxidized gold nanoparticles: a catalytic base-free system for the aerobic homocoupling of alkynes, J. Catal. 315 (2014) 6–14.
[71] H.-J. Freund, M. Heyde, N. Nilius, S. Schauermann, S. Shaikhutdinov, M. Sterrer, Model studies on heterogeneous catalysts at the atomic scale: from supported metal particles to two-dimensional zeolites, J. Catal. 308 (2013) 154–167.
[72] R. Tiruvalam, Q. He, A.A. Herzing, J. Pritchard, N. Dimitratos, J.A. Lopez-Sanchez, J.K. Edwards, A.F. Carley, G.J. Hutchings, C.J. Kiely, Some recent advances in gold-based catalysis facilitated by aberration corrected analytical electron microscopy, J. Phys. Conf. Ser. 371 (2012), 012028.
[73] J.K. Edwards, B.E. Solsona, P. Landon, A.F. Carley, A. Herzing, C.J. Kiely, G. J. Hutchings, Direct synthesis of hydrogen peroxide from H2 and O2 using TiO2-supported Au–Pd catalysts, J. Catal. 236 (2005) 69–79.
[74] M. Boronat, A. Corma, Oxygen activation on gold nanoparticles: separating the influence of particle size, particle shape and support interaction, Dalton Trans. 39 (2010) 8538–8546.
[75] A.J. Logsdail, L.O. Paz-Bórbon, C.A. Downing, DFT-computed trends in the properties of bimetallic precious metal nanoparticles with Core@Shell Segregation, J. Phys. Chem. C 122 (2018) 5721–5730.
[76] P. Tian, D. Ding, Y. Sun, F. Xuan, X. Xu, J. Xu, Y.-F. Han, Theoretical study of size effects on the direct synthesis of hydrogen peroxide over palladium catalysts, J. Catal. 369 (2019) 95–104.
[77] M. Boronat, A. Leyva-Pérez, A. Corma, Theoretical and experimental insights into the origin of the catalytic activity of subnanometric gold clusters: attempts to predict reactivity with clusters and nanoparticles of gold, Acc. Chem. Res. 47 (2014) 834–844.
[78] A. Roldán, S. González, J.M. Ricart, F. Illas, Critical size for O_2 dissociation by Au nanoparticles, ChemPhysChem 10 (2009) 348–351.
[79] A. Staykov, D. Derekar, K. Yamamura, Oxygen dissociation on palladium and gold core/shell nanoparticles: Staykov et al, Int. J. Quantum Chem. 116 (2016) 1486–1492.
[80] J.B.A. Davis, F. Baletto, R.L. Johnston, The effect of dispersion correction on the adsorption of CO on metallic nanoparticles, J. Phys. Chem. A 119 (2015) 9703–9709.
[81] T. Whittaker, K.B.S. Kumar, C. Peterson, M.N. Pollock, L.C. Grabow, B.D. Chandler, H_2 oxidation over supported Au nanoparticle catalysts: evidence for heterolytic H_2 activation at the metal–support interface, J. Am. Chem. Soc. 140 (2018) 16469–16487.
[82] P. Tian, X. Xu, C. Ao, D. Ding, W. Li, R. Si, W. Tu, J. Xu, Y.-F. Han, Direct and selective synthesis of hydrogen peroxide over palladium-tellurium catalysts at ambient pressure, ChemSusChem 10 (2017) 3342–3346.